Plasmonic Nanogap Grid Arrays for Tunable SERS Enhancement and Strain-Induced Shifts in 2D Materials

CHENG CHEN,[1] SUNGHWAN KIM,[1] SATYABRAT BEHERA,[1] HWANHEE KIM,[1] SEON NAMGUNG,[1] HYEONG-RYEOL PARK,[1*] AND DUKHYUNG LEE[2*]

[1]*Department of Physics, Ulsan National Institute of Science and Technology, Ulsan 44919, Republic of Korea*

[2]*School of Applied and Engineering Physics, Mohammed VI Polytechnic University, Ben Guerir 43150, Morocco*

[1*]nano@unist.ac.kr

[2*]dukhyung.lee@um6p.ma

Abstract: Gap plasmons in metallic nanogaps confine electromagnetic fields to sub-wavelength volumes, offering a significant advantage for surface-enhanced Raman scattering (SERS). The performance of a nanogap SERS substrate relies heavily on its geometry, which can be customized using e-beam lithography with high fidelity and resolution. In this work, we fabricated nanogap grid arrays with various gap widths between 7 and 60 nm and periods of 150, 200, and 300 nm using e-beam lithography and explored their geometrical effects on SERS enhancement and strain-induced shifts in 2D materials. The measured transmission and reflection spectra show good agreement with simulations, implying electric field enhancement due to gap plasmon excitation. In SERS experiments on rhodamine 6G with varying gap widths, we demonstrated that the field enhancement and the resulting SERS signal increase with decreasing gap width. Meanwhile, a comparison of the SERS signals with different periods revealed a trade-off between proximity effects and nanogap density. Furthermore, we transferred a few layers of molybdenum disulfide (MoS_2) onto nanogap grid arrays, and then observed a redshift in the peaks of the SERS on these samples, revealing that larger gap widths induce greater stretching in the 2D material. Our findings provide insights into optimizing nanogap SERS substrates and leveraging grid structures to induce strain effects in 2D materials, highlighting potential applications in biomolecular sensing, chemical detection, and optoelectronics.

1. Introduction

Surface-enhanced Raman scattering (SERS) has become a fundamental analytical technique for molecular detection, leveraging the interaction between light and metallic nanostructures to amplify weak Raman signals by several orders of magnitude [1-8]. At its core, SERS relies on two primary mechanisms: electromagnetic enhancement [9-11], driven by localized surface

plasmon resonance (LSPR) at nanoscale metallic interfaces, and chemical enhancement [11-16], arising from charge transfer between adsorbed molecules and the substrates. The former mechanism has been extensively studied, with research demonstrating that the geometry of nanostructures directly influences the electromagnetic field strength and the SERS enhancement factor, as exemplified by double-Fano-resonant SERS chips providing broadband tunability and refractive-index robustness [17]. Metallic nanogaps supporting gap plasmons [18-20] serve as key structures for enhancing SERS, with narrower gaps yielding stronger field enhancement, especially when the gap width is below 10 nm [21-26]. This potential for performance enhancement through structural optimization endows nanogap SERS substrates with broad application prospects across multiple fields. For instance, SERS using nanogaps has enabled ultrasensitive identification of biomolecules like proteins [27] and nucleic acids [28], detection of pesticides[29, 30] at trace concentrations, and even real-time monitoring of viral particles [31]. Nanogap SERS substrates also offer intriguing tunability on the optoelectronic properties of 2D materials by introducing mechanical strain [32], identifiable through SERS peak shifts. Therefore, the widespread adoption of SERS hinges on overcoming a critical challenge: the reproducible fabrication of densely packed nanogaps with high degree of precision and uniformity to maximize hotspot intensity and density.

Diverse fabrication methods have been devised for sub-10 nm gaps, each with its own trade-offs, advantages, and limitations. Nanoparticle self-assembly [33-35] and DNA origami [36, 37] provide cost-effective approaches but lack precise control over gap geometry and spatial distribution. Strain-induced nanocracking [38] enables wafer-scale nanogap arrays but often suffers from irregular edges and limited pattern diversity. Atomic layer deposition (ALD) [39, 40] and nanoskiving [41] provide excellent geometric precision but come with the drawback of multi-step processes and stringent material compatibility constraints. In terms of process control, conventional lithography techniques using resists remain superior, offering minimal uncertainties and high reproducibility, which is especially crucial for sensing applications. Indeed, nanogap SERS substrates fabricated by deep UV lithography were demonstrated with excellent SERS reproducibility [42]. Since e-beam lithography (EBL) can achieve resolutions even below 10 nm, optimizing high-density nanogap SERS substrates through EBL patterning is highly advantageous.

In this study, we demonstrated the reliable fabrication of grid nanogap arrays using EBL combined with ion etching and evaluated their performance for SERS applications based on geometrical factors. We performed a straightforward three-step fabrication process involving gold deposition, EBL patterning, and ion etching to produce square grid nanogap arrays with gap widths ranging from 7 to 60 nm and periods of 150, 200, and 300 nm. Transmission and reflection spectra measured in the wavelength range of 500 to 1000 nm showed good agreement with the numerical simulations, suggesting gap plasmon excitation and the Fabry–Pérot resonance. SERS performances were investigated using Rhodamine 6G (R6G) and

molybdenum disulfide (MoS_2) with the excitation wavelength of 633 nm. It was found that Raman intensity can be significantly enhanced by reducing the gap width, while tensile strain in transferred MoS_2, indicated by Raman peak redshifts, can be induced by employing larger gap widths. Our approach highlights how simple and reproducible EBL patterning can facilitate the practical implementation of nanogap SERS substrates, optimizing the plasmonic hotspots and allowing strain engineering of 2D materials.

2. Grid nanogap array fabrication and characterization

Square grid nanogaps were fabricated by a three-step top-down method, of which process is schematically described in Fig. 1(a). First step is metal deposition: a quartz substrate with a 500 um-thickness was cleaned sequentially using acetone, methanol, and DI water by sonication. After cleaning, a Cr(3nm)/Au(50nm) thin film was deposited on the quartz substrate by e-beam evaporator. Second step is EBL: Polymethyl methacrylate (PMMA) was spin coated on the gold film and baked for 1 minute at 180 ℃, followed by e-beam writing and resist development to form square grid patterns in the PMMA layer. Each array pattern was designed to have an area of 20 um × 20 um. Third step is ion etching: the grid patterns were transferred as gold nanogap arrays by argon ion etching. Nanogap arrays were fabricated in with various periods (150, 200, and 300 nm) and gap widths (range from 7 to 60 nm). This fabrication process utilizes standard EBL equipment, offering deterministic control and high reproducibility.

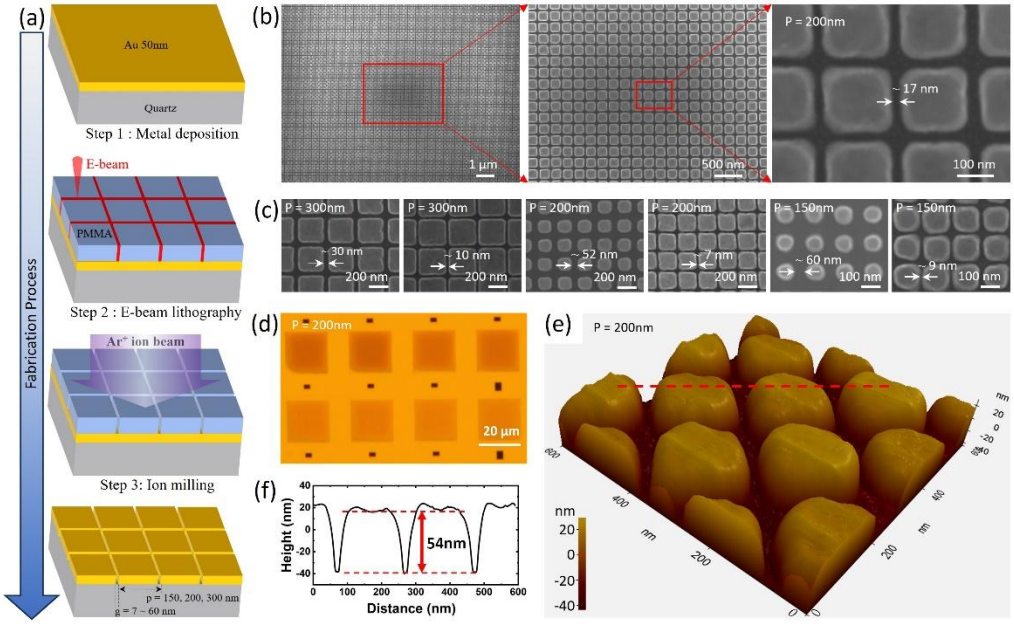

Fig. 1. Fabrication process and topology characterization. (a) Schematic flow of the square grid nanogap fabrication process. A layer of Cr(3nm)/Au(50nm) is deposited on a 500 μm thick quartz substrate, followed by e-beam lithography process to define the grid patterns. Subsequent argon ion etching transfers these patterns into the gold nanogaps. (b) Top view SEM images of a

nanogap array with a 200 nm period and a 16 nm gap width. (c) SEM images of nanogap arrays of various periods and gap widths. (d) Optical microscope image of 200 nm-period nanogap arrays, where the gap width decreases from left to right and top to bottom. (e) Topographic AFM image of a square grid nanogap. (f) Cross-sectional AFM profile of the red dot line in (e).

Dimensions of the nanogap arrays were identified by field emission scanning electron microscopy (FE-SEM) and atomic force microscopy (AFM). FE-SEM images of a grid nanogap in Fig. 1(b) show that the nanogaps have good uniformity across the entire array, except the gap intersections positions due to the proximity effect [43, 44] during the EBL process. We estimated the gap widths of the fabricated arrays from the FE-SEM images, with selected examples shown in Fig. 1(c). The difference in gap widths between the arrays manifested as visible color change, as seen in the optical microscope image (Fig. 1(d)) where the gap width gradually varies across eight arrays. To further verify the formation of the nanogap arrays, three-dimensional morphology of a nanogap array of a 33 nm gap width was characterized using a sharp AFM probe (tip radius of curvature < 5 nm), as shown in Fig. 1(e). The cross-sectional profile in Fig. 1(f) shows a ~10 nm-wide plateau in the gap region, suggesting that the probe reached the bottom of the gap, although the high aspect ratio of the gap limited precise tracking of the full 33 nm width. The gold island thickness of 54 nm confirms that the metal layer was deposited with the intended thickness and that the ion milling process was terminated at the appropriate time.

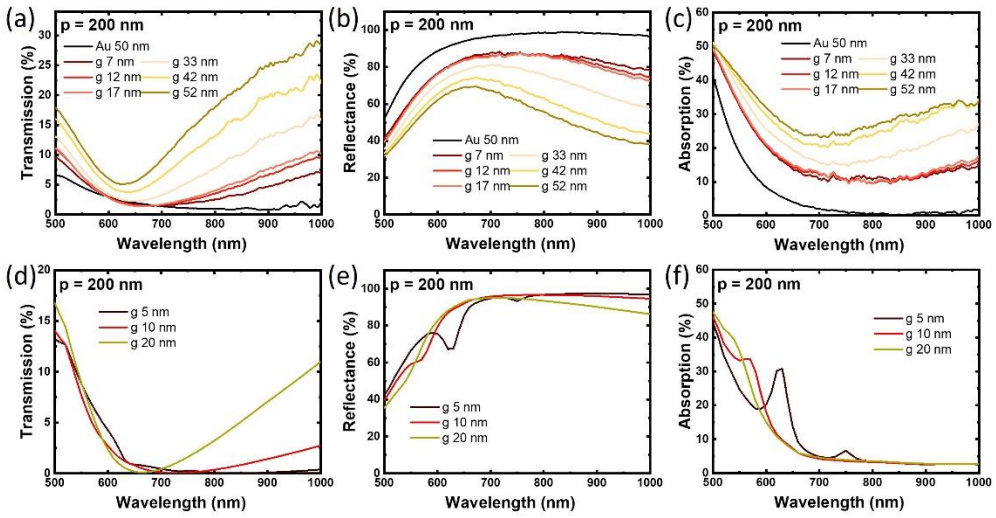

Fig. 2. Experiment and simulation results of transmission, reflectance and absorption spectra of nanogap arrays with a 200 nm period. (a, b, c) Measured spectra with gap widths of 7, 12, 17, 33, 42 and 52 nm. Absorption spectra were calculated by $A = 1 - T - R$. The black curves represent the case of an unpatterned gold film, for comparison purposes. (d, e, f) Simulated spectra of nanogap arrays with gap widths of 5, 10, and 20 nm, showing a consistent tendency with the experiment.

We investigated the optical properties of the array samples using a microspectrometer in the wavelength range of 500 to 1000 nm. Since each pattern area is 20 μm × 20 μm, we used an aperture to collect signals only from the central region with a diameter of 10.8 μm. Transmission and reflection spectra of the nanogap arrays were normalized by using transmission spectrum of a bare quartz substrate and reflection spectrum of a 120 nm thick silver film, respectively. Absorption spectra were calculated by the formula $A = 1 - T - R$. The transmission, reflection, and absorption spectra for the 200 nm period arrays are plotted in Figs. 2(a-c). In the wavelength range above 600 nm, transmission increases while reflection decreases with increasing wavelength, consistent with the fact that a dense slit array achieves near-perfect transmission [45]. This trend becomes more pronounced in arrays with larger gap widths. The increase in transmission and absorption in the wavelength range under 600 nm can be attributed to the interband transitions of gold.

To understand the optical properties, we performed finite element method simulations (COMSOL Multiphysics). We note that, in the simulations, the corners at the gap intersections were rounded with a radius of 20 nm to account for the proximity effect, while all other metal edges were rounded with a 1 nm radius to prevent singularities, as shown in Figs. 3(d,e). The overall trends of the simulated spectra (Figs. 2(d–f)) are similar to those observed in the experimental results. In the simulated reflection and absorption spectra for the 5 nm gap width, we can identify a distinct resonance at ~630nm. The resonance is also observed, albeit more weakly, at shorter wavelengths for gap widths of 10 nm and 20 nm. This blueshift with increasing gap width suggests that this resonance is a Fabry–Pérot resonance of the gap plasmon [46]. This resonance is not clearly observed in the experimental data, possibly due to structural irregularities such as slight deviations in gap width and the wider top openings in the fabricated samples. Since Fabry–Pérot resonances should be exist in all the nanogap variations of a finite length, it is reasonable to infer that the resonance peak observed in the idealized simulation became distributed and broadened in the real samples, thereby smearing out the distinct spectral feature.

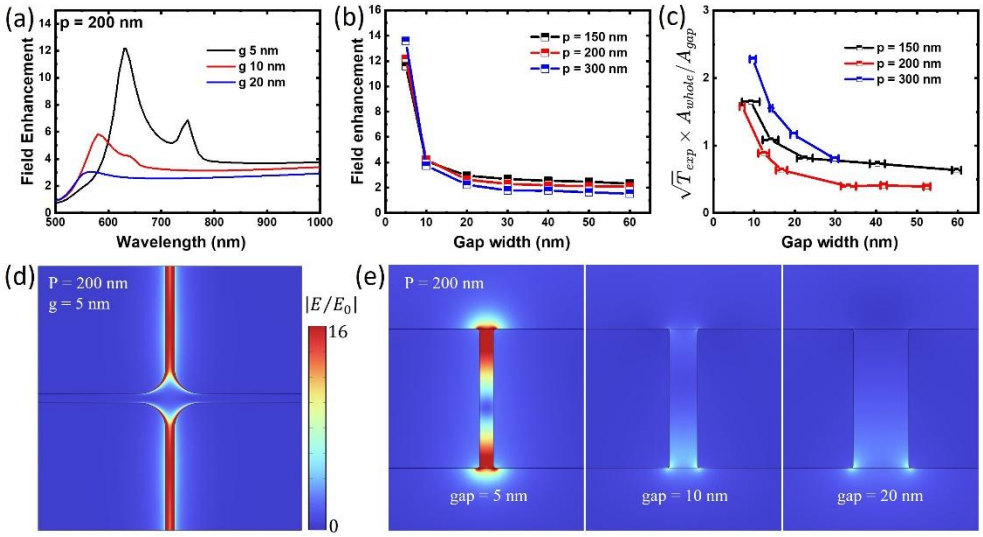

Fig. 3. Field enhancement due to the gap. (a) Simulated electric field enhancement ($|E/E_0|$) spectra of 200 nm period nanogap arrays with 5, 10, and 20 nm-gap widths. Average was taken at the bottom surface of the gap. (b) Simulated field enhancement versus gap width at the wavelength of 633 nm at which we conducted Raman spectroscopy. (c) Experimental estimation of field enhancement versus gap width at the wavelength of 633 nm. The estimation is given by $\sqrt{T_{exp}} \times A_{whole}/A_{gap}$ where T_{exp} is the experimental transmission value given in Fig. 2(a), A_{whole} is the whole area, and A_{gap} is the gap area. (d) Top view of simulated electric field ($|E/E_0|$) distribution at the bottom surface with the 633 nm excitation wavelength. The nanogap width and period are 5 nm and 200 nm, respectively. (e) Cross-sectional distributions of simulated electric field at the 633 nm excitation for the gap widths of 5, 10 and 20 nm. The color scale is the same as (d).

We examined the electric field enhancement, which is crucial for effective SERS performance. Figure 3(a) presents the simulated field enhancement as a function of wavelength for nanogap arrays with a 200 nm period, showing that the field enhancement increases significantly as the gap width decreases, accompanied by a blueshift in the resonance wavelength. Since our SERS measurements were conducted at the wavelength of 633 nm, the field enhancement at this wavelength was plotted as a function of gap width in Fig. 3(b) for the three different periods. All three periods yield nearly identical curves, indicating that the field enhancement at 633 nm is primarily determined by the gap width rather than the periodicity. Based on the Kirchhoff integral formalism, the field enhancement at 633 nm can also be estimated from the experimental transmission T_{exp} using the expression $\sqrt{T_{exp}} \times A_{whole}/A_{gap}$ where A_{whole}/A_{gap} denotes the coverage ratio of the gap region [45, 47]. This experimental estimation shown in Fig. 3(c) further confirms that the electric field is enhanced as the gap width decreases.

The origin of the field enhancement at the 633 nm wavelength becomes clear when inspecting field distributions. Gap plasmons require an electric-field component across the slit and corresponding charge accumulation on the opposing sidewalls. Under x-polarized illumination, the induced current in the gold patterns flows in the direction of the incident polarization, leading to charge deposition on the sidewalls perpendicular to the polarization axis. As a result, only nanogaps oriented perpendicular to the incident polarization can support strong gap plasmon excitation [24, 48]. The top-view field map in Fig. 3(d) shows that field enhancement occurs exclusively in nanogaps oriented perpendicular to the incident x-polarization, while those aligned parallel to it exhibit negligible fields, as expected for gap plasmon excitation. Figure 3(e) presents cross-sectional field maps at the midplanes for gap widths of 5, 10, and 20 nm. The field map for the 5 nm width (left) clearly shows the excitation of a Fabry–Pérot resonance of the gap plasmon, generating two electric hot spots at the top and bottom openings. As increasing the gap width (center, right), the Fabry–Pérot resonance condition is gradually mismatched at the 633 nm wavelength, resulting in the smaller field enhancement. Although the fabricated samples have some structural irregularities smearing out the distinct peak, it is reasonable to assume that SERS performance still benefits from some degree of field enhancement due to gap plasmon excitation and the Fabry–Pérot resonance, particularly for gap widths below 10 nm, even if not as strong as in the simulations.

3. SERS performance and geometrical factors

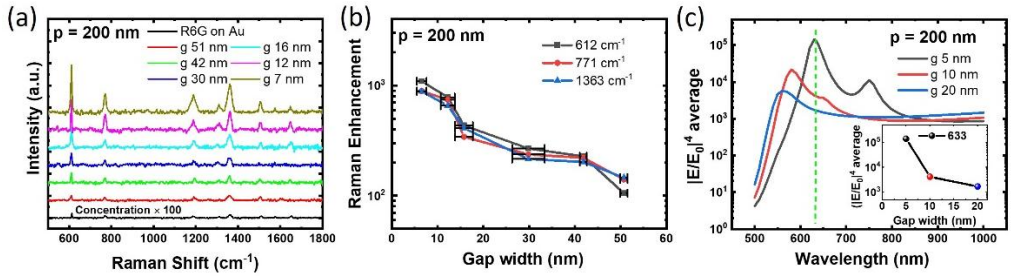

Fig. 4. The effect of gap width on the SERS spectra from the nanogap arrays of a 200 nm period. (a) Measured SERS spectra of R6G molecules under 633 nm laser excitation. R6G aqueous solution of 10^{-5} M was drop-casted on the nanogap samples. For comparison, the black curve shows the Raman spectrum of 10^{-3} M R6G deposited on a gold film without nanogaps. (b) Raman enhancement factors for the three main characteristic peaks calculate by $\left(I_{nanogap}/I_{film}\right) \times (10^{-3}\mathrm{M}/10^{-5}\mathrm{M})$. (c) Simulated $|E/E_0|^4$ averaged over the whole surface. The green dashed line indicates the 633 nm wavelength. The inset displays the dependence on the gap width at 633 nm.

Performance of nanogap arrays as SERS substrates and its dependence on the gap width were investigated. We selected R6G as a probe molecule due to its widespread use in previous SERS studies [49]. R6G solutions of a concentration of 10^{-5} M were prepared using ethanol as the

solvent. Drop-casted R6G molecules on nanogap arrays were excited by an unpolarized 633 nm laser with the power of 1 mW and the laser spot size of ~1 μm. We collected the SERS spectra over the wavenumber range of 500–1800 cm^{-1} and obtained the average spectrum from 5 measurement positions randomly selected within each array (Supplementary Information S1: repeated Raman measurements for representative nanogap arrays with different gap widths and periods). Figure 4(a) presents the SERS spectra from nanogap arrays with a 200 nm period, along with that from an unpatterned gold film (black line), for which a higher R6G concentration of 10^{-3} M was used due to the weak signal. Compared to the SERS signal from the unpatterned gold film, the nanogap arrays exhibited significantly enhanced responses, with the signal progressively intensifying as the gap width decreased from 52 nm to 7 nm. Figure S1(c) shows the 5 Raman measurements within the array of a 7 nm gap width, and the relative standard deviations (RSDs) for the three prominent peaks at 612 cm^{-1}, 771 cm^{-1}, and 1363 cm^{-1} are 3.08%, 2.66% and 2.40%, respectively, demonstrating good reproducibility. We calculated the Raman enhancement factors for the three peaks at 612 cm^{-1}, 771 cm^{-1}, and 1363 cm^{-1} as a function of gap width, as shown in Fig. 4(b). All three peaks displayed an exponential increase with decreasing gap width, consistent with findings from other studies [4], and achieved enhancement factors of ~10^3 at the gap width of 7 nm. We note that many previous SERS studies estimated enhancement factors by considering only molecules located within hotspot volumes. In contrast, we estimated overall SERS enhancement factors of the arrays by accounting for the total signal, including contributions from both hotspot and non-hotspot regions. While this method yields lower enhancement factors compared to hotspot-only estimates, it provides a more realistic assessment under practical conditions where analytes are distributed across the entire surface. Because SERS signal is generally proportional to the fourth power of the field enhancement ($|E/E_0|^4$), we examined the $|E/E_0|^4$ spectra for gap widths of 5, 10, and 20 nm through simulations, as plotted in Fig. 4(c). Here, we averaged $|E/E_0|^4$ over the entire air-exposed surface area of the simulated unit cell, including the top and side gold surfaces and the substrate surfaces at the gap openings, considering the case of uniform spreading of molecules. The inset of Fig. 4(c) shows a drastic increase in $|E/E_0|^4$ at the 633 nm wavelength as the gap width narrows, further confirming that the performance of nanogap arrays as SERS substrates is highly dependent on the gap width. We remark that, since the Fabry–Pérot resonance lies near 633 nm, other commonly used laser wavelengths (532 nm and 785 nm) are less suitable for achieving such a pronounced increase (Supplementary Information S2).

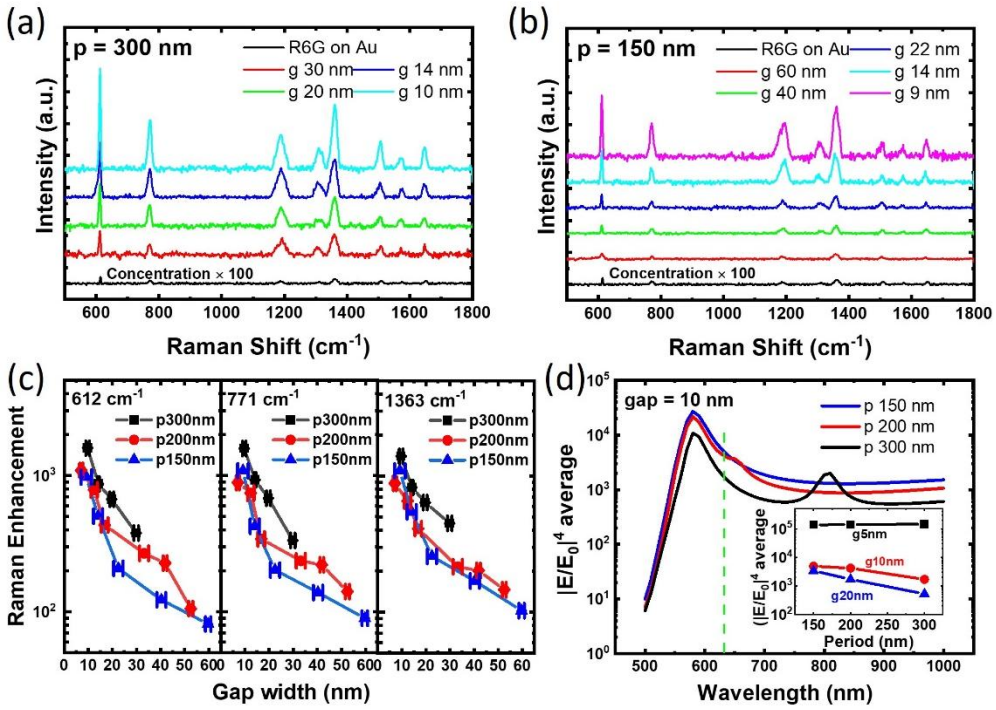

Fig. 5. SERS spectra measured with nanogap arrays of different periods. (a) SERS for the 300 nm period. (b) SERS for the 150 nm period. The measurement method is the same as that for Fig. 4. (c) Raman enhancement factors obtained for the three distinct periods of 150, 200, and 300 nm. (d) Simulated $|E/E_0|^4$ average for the three periods with a 10 nm-gap width. The inset displays the dependence on the period at 633 nm.

The influence of the period on SERS performance was also investigated by measuring the R6G SERS spectra from the nanogap arrays with periods of 300 nm and 150 nm (Figs. 5(a,b)). Similar to the 200 nm period, both arrays exhibited increased Raman signals as the gap width decreased. For all three periods of 150, 200, and 300 nm, the Raman enhancement factors of the main peaks were calculated and plotted in Fig. 5(c). Contrary to expectations based on the areal density of nanogaps, all peaks exhibited a trend where longer periods resulted in higher Raman enhancement factors. This may be attributed to structural irregularities in the fabricated samples, as evidenced by comparison with the simulation results. Figure 5(d) presents the simulated $|E/E_0|^4$ spectra for the three periods, all with a 10 nm gap width. It shows that a smaller period can yield a higher Raman signal, as expected from the increased density of nanogaps. The additional peak near 810 nm for the 300 nm period is attributed to an in-plane oscillation mode of the gap plasmon (Supplementary Information S3). The inset of Fig. 5(d) depicts the relationship between the average $|E/E_0|^4$ at the 633 nm wavelength and the period for different gap widths. The 20 nm gap width exhibits the same trend as the 10 nm case. For the 5 nm gap, slight weakening of gap plasmon excitation (Fig. 3(b)) offsets the effect of

increased nanogap density, resulting in nearly constant values. This discrepancy between the experimental (Fig. 5(c)) and simulated (Fig. 5(d)) results suggests that the array period influences SERS performance through two competing effects: (i) a reduced period increases hotspot density, whereas (ii) fabrication fidelity generally degrades at smaller periods as the higher number of grid intersections deteriorates EBL proximity effects. At these intersections, dose spillover can lead to wider top openings or edge rounding, thereby reducing local fields and increasing spectral broadening. The observation of higher SERS signals at longer periods in the experiment can thus be attributed to effect (ii) outweighing effect (i) in our samples. Therefore, a balance between nanogap density and fabrication precision should be considered to optimize SERS performance. Notably, the EBL process here was carried out at an accelerating voltage of 30 kV, whereas higher voltages could potentially provide improved resolution. Moreover, there remains considerable potential for optimization of EBL parameters, such as resist thickness, line does, e-beam current and development time [50, 51]. By mitigating proximity effects and improving resolution, even higher performance could be expected for shorter periods.

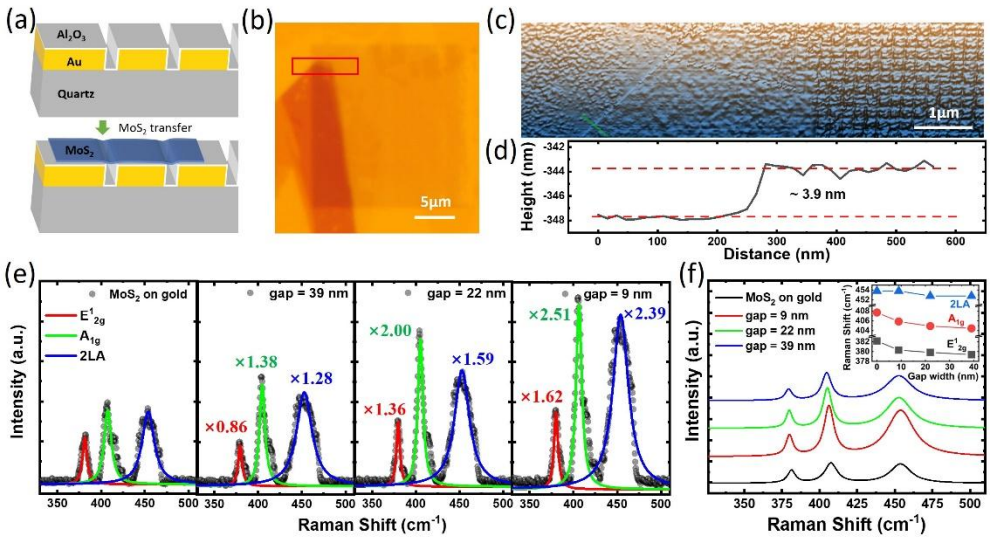

Fig. 6. SERS of few-layer MoS_2 transferred on nanogap arrays. (a) Schematics of MoS_2 transfer. Firstly, 4 nm Al_2O_3 was conformally deposited on nanogap arrays by ALD and followed by dry transfer of few layer MoS_2. (b) Optical microscope image of a nanogap array partially covered by MoS_2. (c) AFM image inside the red square region in (b). (d) Cross-sectional AFM profile along the green line in (c), showing that the thickness of MoS_2 is 3.9nm. (e) Raman spectra of MoS_2 on a gold film without nanogaps and on nanogap arrays of various gap widths. The period of all arrays is 200 nm. The solid lines are Lorentzian fittings for each peak. (f) Comparison between the fitting curves of the Raman spectra. The inset shows the peak positions as functions of the gap width. The gap width of 0 indicates the unpatterned gold case.

To explore the applicability of grid nanogap structures to 2D materials, we performed SERS measurements on transferred MoS_2. Before transferring MoS_2, a 4 nm Al_2O_3 layer was conformally deposited onto 200 nm period nanogap arrays by ALD to prevent direct charge transfer and electronic interactions between MoS_2 and gold. MoS_2 was transferred from its bulk form onto the nanogap arrays via a dry transfer method using polydimethylsiloxane (PDMS), as illustrated in Fig. 6(a). Successful MoS_2 transfer was confirmed by optical microscopy, as in the example shown in Fig. 6(b), where a multilayer MoS_2 region is observed overlaid on the left part of the nanogap array. We conducted AFM scanning to measure the thickness of the transferred MoS_2. Figure 6(c) is the AFM image corresponding to the red box region in Fig. 6(b). In the AFM image, we can distinguish three regions from left to right: the unpatterned gold, transferred MoS_2, and the nanogap array. Figure 6(d) is the cross-sectional AFM profile along the green line in Fig. 6(c), transversing the MoS_2 edge on the unpatterned gold. As shown in Fig. 6(d), the transferred MoS_2 had a thickness of 3.9 nm, corresponding to 5 or 6 layers. The Raman spectra of the samples were measured using 633 nm excitation, and the results are shown in Fig. 6(e). From left to right, the spectra correspond to MoS_2 on the gold film and on nanogap arrays with gap widths of 39 nm, 22 nm, and 9 nm, respectively. All spectra were deconvoluted using three Lorentzian peaks (solid lines) to determine peak positions. The Raman spectrum of MoS_2 on the gold film exhibited three modes: E^1_{2g} at 382.16 cm^{-1}, A_{1g} at 407.70 cm^{-1}, and 2LA at 453.82cm^{-1}. The frequency difference between the E^1_{2g} and A_{1g} peaks is 25.54 cm^{-1}, which aligns with the measured thickness of 3.9 nm [52]. Compared to the Raman peaks of MoS_2 on the gold film, those from the nanogap arrays exhibited enhancement. Considering that an Al_2O_3 spacer was introduced between gold and MoS_2 to suppress charge transfer, the observed effect can be attributed to electromagnetic enhancement. This enhancement increased with decreasing gap width, as expected from the electric field enhancement. At the gap width of 9 nm, the peak intensities of E^1_{2g}, A_{1g}, and 2LA are enhanced by factors of 1.62, 2.51, and 2.39, respectively. The relatively modest enhancement may be related to the presence of the Al_2O_3 layer, which positions MoS_2 above the nanogaps rather than directly within the hotspot region. The observed differences in enhancement factors among Raman modes can be attributed to mode-specific coupling with distinct components of the local field and the effect of exciton-plasmon coupling in MoS_2 [53]. Similar non-synchronous enhancements have also been reported in previous studies [32].

One interesting feature of this MoS_2/nanogap system is redshift of the Raman peaks. Owing to the presence of nanogaps, transferred MoS_2 experiences localized tensile strain across the suspended regions [54, 55], and the magnitude of this strain increases with gap width. It has been well established that tensile strain reduces interatomic restoring forces and softens phonon modes, causing redshifts of Raman modes [56, 57]. As illustrated in Fig. 6(f) and the inset, redshift became more pronounced as the gap widened, consistent with the corresponding increase in strain. Among the three peaks, the A_{1g} mode exhibited the most pronounced redshift,

shifting from 407.70 cm^{-1} on the gold film to 404.46 cm^{-1} at the gap width of 39 nm, corresponding to a 0.79% change. The E^1_{2g} and 2LA peaks at the 39 nm gap width showed redshifts of 0.73% and 0.23%, respectively. Similar strain-induced Raman peak shifts have been reported in other systems [32]. Since the gap width can be tuned at the nanometer-scale using EBL, our nanogap grid arrays can be utilized for precise strain engineering of 2D materials.

4. Conclusions

We fabricated nanogap grid arrays using EBL and ion etching. After confirming the successful formation of densely packed nanogaps with nanometer-scale precision, we evaluated their SERS performance using R6G and MoS_2 as model materials while systematically varying the gap widths (7–60 nm) and periods (150–300 nm) across this wide range. By narrowing the gap width down to just a few nanometers, we achieved Raman enhancement factors of approximately 10^3, attributed to gap plasmon excitation and Fabry–Pérot resonance. However, we found that the array period must be carefully optimized due to proximity effects during fabrication. Additionally, redshifts in the MoS_2 Raman peaks revealed that the nanogap arrays induce tensile strain in the transferred 2D materials, and this strain can be tuned by adjusting the gap width, highlighting the potential of nanogap arrays for investigating 2D materials coupled with surface plasmons [58, 59]. We also note that introduction of 2D materials with chemical SERS enhancement is anticipated. Our study offers both fundamental insights and practical guidance for leveraging nanogap arrays in SERS applications, with promising implications for optical sensing and optoelectronics.

Funding. National Research Foundation of Korea (NRF) grant funded by the Korean government (2022M3H4A1A04096465, RS-2023-00257666, RS-2024-00353252, RS-2024-00454894, RS-2025-02272971, and RS-2025-06642983); 2025 Research Fund of Ulsan National Institute of Science and Technology (1.250007.01).

Disclosures. The authors declare no conflicts of interest.

Data Availability. Data used in this study are available from the corresponding author upon reasonable request.

References

1. Y. Jiao, J. D. Ryckman, P. N. Ciesielski, et al., "Patterned nanoporous gold as an effective SERS template," Nanotechnology **22**, 295302 (2011).
2. D. Wang, W. Zhu, Y. Chu, et al., "High directivity optical antenna substrates for surface enhanced Raman scattering," Adv. Mater. **24**, 4376–4380 (2012).
3. P. Kuhler, M. Weber, and T. Lohmuller, "Plasmonic nanoantenna arrays for surface-enhanced Raman spectroscopy of lipid molecules embedded in a bilayer membrane," ACS Appl. Mater. Interfaces **6**, 8947–8952 (2014).
4. W. Zhu and K. B. Crozier, "Quantum mechanical limit to plasmonic enhancement as observed by surface-enhanced Raman scattering," Nat. Commun. **5**, 5228 (2014).
5. X. Li, X. Ren, Y. Zhang, et al., "An all-copper plasmonic sandwich system obtained

through directly depositing copper NPs on a CVD grown graphene/copper film and its application in SERS," Nanoscale **7**, 11291–11299 (2015).

6. Y. Zhao, D. Yang, X. Li, et al., "Toward highly sensitive surface-enhanced Raman scattering: the design of a 3D hybrid system with monolayer graphene sandwiched between silver nanohole arrays and gold nanoparticles," Nanoscale **9**, 1087–1096 (2017).
7. H. Le-The, J. J. A. Lozeman, M. Lafuente, et al., "Wafer-scale fabrication of high-quality tunable gold nanogap arrays for surface-enhanced Raman scattering," Nanoscale **11**, 12152–12160 (2019).
8. Z. Zuo, S. Zhang, Y. Wang, et al., "Effective plasmon coupling in conical cavities for sensitive surface enhanced Raman scattering with quantitative analysis ability," Nanoscale **11**, 17913–17919 (2019).
9. D. L. Jeanmaire and R. P. Van Duyne, "Surface Raman spectroelectrochemistry: Part I. Heterocyclic, aromatic, and aliphatic amines adsorbed on the anodized silver electrode," J. Electroanal. Chem. **84**, 1–20 (1977).
10. P. Dawson, D. Frey, V. Kalathingal, et al., "Novel routes to electromagnetic enhancement and its characterisation in surface- and tip-enhanced Raman scattering," Faraday Discuss **205**, 121–148 (2017).
11. T. Itoh, M. Prochazka, Z. C. Dong, et al., "Toward a New Era of SERS and TERS at the Nanometer Scale: From Fundamentals to Innovative Applications," Chem. Rev. **123**, 1552–1634 (2023).
12. L. Jensen, C. M. Aikens, and G. C. Schatz, "Electronic structure methods for studying surface-enhanced Raman scattering," Chem. Soc. Rev. **37**, 1061–1073 (2008).
13. M. G. Albrecht and J. A. Creighton, "Anomalously intense Raman spectra of pyridine at a silver electrode," J. Am. Chem. Soc. **99**, 5215–5217 (1977).
14. S. Guo, H. Cao, Y. Yang, et al., "Silver nanoparticles modified on cicada wings affect fluorescence and Raman signals based on electromagnetic and chemical enhancement mechanisms," Opt. Laser. Technol. **181**, 111912 (2025).
15. G. Fang, X. Lin, J. Wu, et al., "Porous Nanoframe Based Plasmonic Structure With High-Density Hotspots for the Quantitative Detection of Gaseous Benzaldehyde," Small **21**, e2408670 (2025).
16. Y. Wu, T. Sun, M. Shao, et al., "Pyroelectrically Driven Charge Transfer and its Advantages on SERS and Self-Cleaning Property," Laser Photonics Rev. **19**, 2401152 (2024).
17. W. Zhu, H. Wang, Y. Wang, et al., "Multifunctional SERS Chip for Biological Application Realized by Double Fano Resonance," Nanomaterials **14,** 2036 (2024).
18. J. M. Nam, J. W. Oh, H. Lee, et al., "Plasmonic Nanogap-Enhanced Raman Scattering with Nanoparticles," Acc. Chem. Res. **49**, 2746–2755 (2016).

19. P. Gu, W. Zhang, and G. Zhang, "Plasmonic Nanogaps: From Fabrications to Optical Applications," Adv. Mater. Interfaces **5**, 1800648 (2018).
20. Y. Li, W. Chen, X. He, et al., "Boosting Light-Matter Interactions in Plasmonic Nanogaps," Adv. Mater. **36**, e2405186 (2024).
21. K. Imura, H. Okamoto, M. K. Hossain, et al., "Visualization of localized intense optical fields in single gold− nanoparticle assemblies and ultrasensitive Raman active sites," Nano Lett. **6**, 2173–2176 (2006).
22. D. K. Lim, K. S. Jeon, H. M. Kim, et al., "Nanogap-engineerable Raman-active nanodumbbells for single-molecule detection," Nat. Mater. **9**, 60–67 (2010).
23. H. Duan, H. Hu, K. Kumar, et al., "Direct and reliable patterning of plasmonic nanostructures with sub-10-nm gaps," ACS nano **5**, 7593–7600 (2011).
24. H. Cai, Y. Wu, Y. Dai, et al., "Wafer scale fabrication of highly dense and uniform array of sub-5 nm nanogaps for surface enhanced Raman scatting substrates," Opt. Express **24**, 20808–20815 (2016).
25. W. Zhu, R. Esteban, A. G. Borisov, et al., "Quantum mechanical effects in plasmonic structures with subnanometre gaps," Nat. Commun. **7**, 11495 (2016).
26. A. E. Cetin, C. Yilmaz, B. C. Galarreta, et al., "Fabrication of Sub-10-nm Plasmonic Gaps for Ultra-Sensitive Raman Spectroscopy," Plasmonics **15**, 1165–1171 (2020).
27. L. M. Almehmadi, S. M. Curley, N. A. Tokranova, et al., "Surface Enhanced Raman Spectroscopy for Single Molecule Protein Detection," Sci. Rep. **9**, 12356 (2019).
28. M. G. Kim, M. Jue, K. H. Lee, et al., "Deep Learning Assisted Surface-Enhanced Raman Spectroscopy (SERS) for Rapid and Direct Nucleic Acid Amplification and Detection: Toward Enhanced Molecular Diagnostics," ACS Nano **17**, 18332–18345 (2023).
29. X. Wang, X. Zhu, Y. Chen, et al., "Sensitive Surface-Enhanced Raman Scattering Detection Using On-Demand Postassembled Particle-on-Film Structure," ACS Appl. Mater. Interfaces **9**, 31102–31110 (2017).
30. P. Zeng, M. Zheng, H. Chen, et al., "Wafer-Level Highly Dense Metallic Nanopillar-Enabled High-Performance SERS Substrates for Molecular Detection," Nanomaterials **13**, 1733 (2023).
31. S. X. Leong, Y. X. Leong, E. X. Tan, et al., "Noninvasive and Point-of-Care Surface-Enhanced Raman Scattering (SERS)-Based Breathalyzer for Mass Screening of Coronavirus Disease 2019 (COVID-19) under 5 min," ACS Nano **16**, 2629–2639 (2022).
32. Y. B. Kim, S. Behera, D. Lee, et al., "Active Surface-Enhanced Raman Scattering Platform Based on a 2D Material-Flexible Nanotip Array," Biosensors **14**, 619 (2024).
33. S.-Q. Zhu, T. Zhang, X.-L. Guo, et al., "Self-assembly of large-scale gold nanoparticle arrays and their application in SERS," Nanoscale Res. Lett. **9**, 1–9 (2014).

34. H. Y. Chen, M. H. Lin, C. Y. Wang, et al., "Large-Scale Hot Spot Engineering for Quantitative SERS at the Single-Molecule Scale," J. Am. Chem. Soc. **137**, 13698–13705 (2015).
35. N. Zhang, H. Hu, M. Singer, et al., "Large-Scale Sub-1-nm Random Gaps Approaching the Quantum Upper Limit for Quantitative Chemical Sensing," Adv. Opt. Mater. **8**, 2001634 (2020).
36. R. Niu, C. Song, F. Gao, et al., "DNA Origami-Based Nanoprinting for the Assembly of Plasmonic Nanostructures with Single-Molecule Surface-Enhanced Raman Scattering," Angew. Chem. **60**, 11695–11701 (2021).
37. R. Niu, F. Gao, D. Wang, et al., "Pattern Recognition Directed Assembly of Plasmonic Gap Nanostructures for Single-Molecule SERS," ACS Nano **16**, 14622–14631 (2022).
38. Q. Zhao, H. Yang, B. Nie, et al., "Wafer-Scale and Cost-Effective Manufacturing of Controllable Nanogap Arrays for Highly Sensitive SERS Sensing," ACS Appl. Mater. Interfaces **14**, 3580–3590 (2022).
39. Y. Q. Cao, K. Qin, L. Zhu, et al., "Atomic-Layer-Deposition Assisted Formation of Wafer-Scale Double-Layer Metal Nanoparticles with Tunable Nanogap for Surface-Enhanced Raman Scattering," Sci. Rep. **7**, 5161 (2017).
40. H. Cai, Q. Meng, H. Zhao, et al., "High-Throughput Fabrication of Ultradense Annular Nanogap Arrays for Plasmon-Enhanced Spectroscopy," ACS Appl. Mater. Interfaces **10**, 20189–20195 (2018).
41. Z. Xiao, C. Chen, G. Xiao, et al., "Customization of Nanogap Arrays Using Stereolithography and Nanoskiving for Surface-Enhanced Raman Scattering," ACS Appl. Nano Mater. **7**, 24235–24245 (2024).
42. U. Dinish, F. C. Yaw, A. Agarwal, et al., "Development of highly reproducible nanogap SERS substrates: Comparative performance analysis and its application for glucose sensing," Biosens. Bioelectron. **26**, 1987–1992 (2011).
43. K. Anbumony and S.-Y. Lee, "True three-dimensional proximity effect correction in electron-beam lithography," J. Vac. Sci. Technol. B **24**, 3115–3120 (2006).
44. M. Urbánek, V. KOLAŘÍK, S. Krátký, et al., "Monte carlo simulation of proximity effect in e-beam lithography," Proc. 5th Int. Conf. NANOCON 2013, 723–726 (2013).
45. S. Kim, D. Kim, Y. Lee, et al., "Broadband high-performance terahertz polarizer based on a dense array of 5 nm gap slit antennas," Opt. Express **30**, 30038–30046 (2022).
46. T. Kang, J. Rhie, J. Park, et al., "Resonance tuning of electric field enhancement of nanogaps," Appl. Phys. Express **8**, 092003 (2015).
47. J. Kyoung, M. Seo, H. Park, et al., "Far field detection of terahertz near field enhancement of sub-wavelength slits using Kirchhoff integral formalism," Opt. Commun. **283**, 4907–4910 (2010).
48. F. García-Vidal, L. Martín-Moreno, E. Moreno, et al., "Transmission of light through

a single rectangular hole in a real metal," Phys. Rev. B **74**, 153411 (2006).

49. Y. X. Zhang, J. Zheng, G. Gao, et al., "Biosynthesis of gold nanoparticles using chloroplasts," Int. J. Nanomedicine **6**, 2899–2906 (2011).
50. V. R. Manfrinato, L. Zhang, D. Su, et al., "Resolution limits of electron-beam lithography toward the atomic scale," Nano Lett. **13**, 1555–1558 (2013).
51. P. Hudek and D. Beyer, "Exposure optimization in high-resolution e-beam lithography," Microelectron. Eng. **83**, 780–783 (2006).
52. H. Li, Q. Zhang, C. C. R. Yap, et al., "From bulk to monolayer MoS_2: evolution of Raman scattering," Adv. Funct. Mater. **22**, 1385–1390 (2012).
53. M.-W. Yu, S. Ishii, S. Li, et al., "Enhancing Raman spectra by coupling plasmons and excitons for large area MoS_2 monolayers," Appl. Surf. Sci. **605**, 154767 (2022).
54. Z. Huang, N. Lu, Z. Wang, et al., "Large-Scale Ultrafast Strain Engineering of CVD-Grown Two-Dimensional Materials on Strain Self-Limited Deformable Nanostructures toward Enhanced Field-Effect Transistors," Nano Lett. **22**, 7734–7741 (2022).
55. J.-P. So, K.-Y. Jeong, J. M. Lee, et al., "Polarization Control of Deterministic Single-Photon Emitters in Monolayer WSe_2," Nano Lett. **21**, 1546–1554 (2021).
56. A. McCreary, R. Ghosh, M. Amani, et al., "Effects of uniaxial and biaxial strain on few-layered terrace structures of MoS_2 grown by vapor transport," ACS nano **10**, 3186–3197 (2016).
57. Y. Wang, C. Cong, C. Qiu, et al., "Raman spectroscopy study of lattice vibration and crystallographic orientation of monolayer MoS_2 under uniaxial strain," Small **9**, 2857–2861 (2013).
58. S. Li, F. Deng, L. Zhou, et al., "Revealing defect-bound excitons in WS(2) monolayer at room temperature by exploiting the transverse electric polarized wave supported by a Si_3N_4/Ag heterostructure," Nanophotonics **12**, 4485–4494 (2023).
59. S. Li, L. Zhou, F. Deng, et al., "Transverse-Electric-Polarized Polaritons Propagating in a WS_2/Si_3N_4/Ag Heterostructure," Laser Photonics Rev. **16**, 2100457 (2022).